The Astrophysical Journal Letters, 1000:L20 (14pp), 2026 March 20 https://doi.org/10.3847/2041-8213/ae4d14
© 2026. The Author(s). Published by the American Astronomical Society.
OPEN ACCESS

Illuminating the Mass Gap through a Deep Optical Constraint on the Neutron Star Merger Candidate S250206dm

Zhengyan Liu[1,2,12], Zelin Xu[1,2,12], Ji-an Jiang[1,2,3], Wen Zhao[1,2], Zhiping Jin[4], Zigao Dai[1,2], Dezheng Meng[1,2], Xuefeng Wu[4], Daming Wei[4], Runduo Liang[1,2,5], Lei He[1,2], Minxuan Cai[1,2], Lulu Fan[1,2,6], Weiyu Wu[1,2], Junhan Zhao[1,2], Ziqing Jia[1,2], Kexin Yu[1,2], Jinjun Geng[4], Di Xiao[4], Feng Li[7], Jinlong Tang[8], Yingxi Zuo[4], Xiaoling Zhang[4], Hao Liu[7], Jian Wang[6,7], Hongfei Zhang[7], Ming Liang[9], Hairen Wang[4], Dazhi Yao[4], Lei Hu[4,10], Xu Kong[1,2,6], Bin Li[4], Ning Jiang[1,2], Tinggui Wang[1,2,6], Zhen Wan[1,2], Yongquan Xue[1,2], Qingfeng Zhu[1,2,6], and Xianzhong Zheng[11]

[1] Department of Astronomy, University of Science and Technology of China, Hefei 230026, People's Republic of China; wzhao7@ustc.edu.cn, daizg@ustc.edu.cn
[2] School of Astronomy and Space Sciences, University of Science and Technology of China, Hefei 230026, People's Republic of China
[3] National Astronomical Observatory of Japan, National Institutes of Natural Sciences, Tokyo 181-8588, Japan
[4] Purple Mountain Observatory, Chinese Academy of Sciences, Nanjing 210023, People's Republic of China; jin@pmo.ac.cn
[5] National Astronomical Observatories, Chinese Academy of Sciences, Beijing 100101, People's Republic of China
[6] Institute of Deep Space Sciences, Deep Space Exploration Laboratory, Hefei 230026, People's Republic of China
[7] State Key Laboratory of Particle Detection and Electronics, University of Science and Technology of China, Hefei 230026, People's Republic of China
[8] Institute of Optics and Electronics, Chinese Academy of Sciences, Chengdu 610209, People's Republic of China
[9] National Optical Astronomy Observatory (NSF's National Optical-Infrared Astronomy Research Laboratory), 950 N Cherry Ave, Tucson, AZ 85726, USA
[10] McWilliams Center for Cosmology, Department of Physics, Carnegie Mellon University, 5000 Forbes Ave, Pittsburgh, PA 15213, USA
[11] Tsung-Dao Lee Institute and Key Laboratory for Particle Physics, Astrophysics and Cosmology, Ministry of Education, Shanghai Jiao Tong University, Shanghai 201210, People's Republic of China
Received 2026 January 12; revised 2026 February 8; accepted 2026 February 16; published 2026 March 16

Abstract

The gravitational wave (GW) event S250206dm, as the first well-localized neutron star (NS) merger candidate potentially located in the mass gap, presented a unique opportunity to probe the electromagnetic signatures from such a system. Here we report a deep, multiband search with the new 2.5 m Wide Field Survey Telescope (WFST), covering ∼64% of the localization region up to a 5σ limiting magnitude of 23 mag. In total, 12 potential candidates have been identified, but none of them are likely related to S250206dm. This nondetection provides the most stringent constraint to date on any associated kilonova. Crucially, an AT 2017gfo-like event at 269 Mpc can be excluded only by WFST observations. Based on ejecta mass limits, a NS-black hole with a large mass ratio ($Q \gtrsim 3.2$) is disfavored. This optically derived constraint on the mass ratio reaches, for the first time, a precision comparable to that inferred from the GW signal. This work presents the best observation of this type of event until now, and demonstrates the power of rapid, deep follow-up observations to constrain the properties of compact binary progenitors, offering key insights into the constituents of the mass gap.

Unified Astronomy Thesaurus concepts: Gravitational wave astronomy (675); Neutron stars (1108)

1. Introduction

Binary neutron star (BNS) and neutron star–black hole (NSBH) mergers are gravitational wave (GW) sources, which can produce electromagnetic (EM) counterparts (B. P. Abbott et al. 2017a; B. D. Metzger 2020; E. Nakar 2020). As the first confirmed BNS merger, the GW event GW170817 (B. P. Abbott et al. 2017b), and the subsequent discovery of its EM counterparts marked a breakthrough, opening the era of multimessenger astronomy. Various EM counterparts to GW170817 have been observed across the entire EM spectrum by numerous facilities. Approximately 2 s postmerger, the Fermi Gamma-ray Space Telescope detected the short gamma-ray burst (sGRB) GRB 170817A, which lasted about 2 s (A. Goldstein et al. 2017; V. Savchenko et al. 2017). Subsequently, ultraviolet, optical, and near-infrared emissions were detected and confirmed as being from a kilonova (KN) coincident with GW170817 and GRB 170817A, designated as AT 2017gfo (D. A. Coulter et al. 2017; E. Pian et al. 2017; N. R. Tanvir et al. 2017; B. J. Shappee et al. 2017). The afterglow emissions were also detected later from X-ray to radio (E. Troja et al. 2017; P. D'Avanzo et al. 2018). The EM counterpart observations, combined with GW data, can be applied to a wide range of scientific studies, such as the origin of heavy elements and constraints on the Hubble constant (B. P. Abbott et al. 2017c; D. Kasen et al. 2017).

A KN is an approximately thermal transient powered by the radioactive decay of *r*-process nuclei, which has long been suspected to be generated in BNS or NSBH mergers (J. M. Lattimer & D. N. Schramm 1974; J. M. Lattimer et al. 1977; D. Eichler et al. 1989). The case of a BNS merger being the progenitor of a KN was confirmed by the multimessenger detection of GW170817. To search for the KNe from NSBH mergers, many observations have been conducted to follow up on NSBH merger candidates during the third observing run (O3) of the LIGO Scientific and Virgo Collaboration (K. Ackley et al. 2020; S. Anand et al. 2020). However, no evident KN from an NSBH merger has been found so far. The nondetection results can be attributed to several main reasons. First, whether tidal disruption occurs in

[12] These authors contributed equally to this work.

Original content from this work may be used under the terms of the Creative Commons Attribution 4.0 licence. Any further distribution of this work must maintain attribution to the author(s) and the title of the work, journal citation and DOI.

an NSBH merger is crucial for producing a KN. Second, a KN is a faint and fast-evolving transient, requiring a timely and deep follow-up to search. Finally, due to the large localization area, it is difficult to cover the entire skymap, even for wide-field telescopes, and searching for KN candidates is also challenging, considering the numerous transients in survey data.

During O4, the LIGO/Virgo/KAGRA Collaboration detected a few GW events likely originating from BNS or NSBH mergers with low false alarm rates (FARs). For NSBH merger candidates, only two events, GW230529_181500 and S250206dm, have a significant probability of retaining neutron star (NS) material outside the merger remnant, potentially producing an EM counterpart (A. G. Abac et al. 2024; LIGO Scientific Collaboration et al. 2025). Additionally, the source classifications of both events are uncertain. They may originate from either a BNS or an NSBH merger, with a high probability of involving one compact object in the so-called lower "mass gap" between the anticipated mass range ($\sim$3 to $\sim 5\,M_{\odot}$) of NSs and that of BHs. The detection of an EM counterpart is an effective way to infer the nature of the composition of the merging system (C. Barbieri et al. 2019; K. Kawaguchi et al. 2020; U. Mali & R. Essick 2025). For GW230529_181500, searching for its EM counterpart is challenging due to its poor localization, spanning a sky area of approximately 24,100 deg^2 at the 90% credible level (A. G. Abac et al. 2024). S250206dm, detected on 2025 February 6, was localized to a 90% credible area of 547 deg^2 (LIGO Scientific Collaboration et al. 2025). The relatively precise localization makes the event a rare opportunity to search for an EM counterpart of an NSBH merger.

In this letter, we present the follow-up campaign conducted by the 2.5 m WFST for S250206dm. In Section 2, we introduce the GW event S250206dm and the follow-up observations by WFST. In Section 3, the procedures of data reduction and EM counterpart search are presented. The probability of discovered candidates as an EM counterpart is discussed in detail in Section 4. In Section 5, based on the nondetection result, the constraints on the potential KN and the progenitor of S250206dm are presented. The comparison with other follow-up campaigns and potential joint constraint are discussed in Section 6. Finally, we conclude our search campaign with constraint results in Section 7. Throughout this study, we adopt a standard ΛCDM cosmology with parameters $H_0 = 67.7\,\mathrm{km\,s^{-1}\,Mpc^{-1}}$, $\Omega_M = 0.31$, and $\Omega_\Lambda = 0.69$ (Planck Collaboration et al. 2020).

2. S250206dm and WFST Follow-up Campaign

The GW event S250206dm was detected by the LIGO-Livingston and LIGO-Hanford detectors at 21:25:30.439 UTC on 2025 February 6, when Virgo and KAGRA were offline.[13] After several alerts being updated (LIGO Scientific Collaboration et al. 2025), S250206dm has a low FAR of 1 per 25.01 yr and may originate from a BNS merger or an NSBH merger, with probabilities of 37% and 55%, respectively. The localization of S250206dm was estimated to have a median luminosity distance of 373 Mpc and a 90% skymap area of 547 deg^2. Other significant compact binary merger events detected in O4, which have at least one NS premerger, are listed in Table 1. The threshold of $P_{\mathrm{BNS}} + P_{\mathrm{NSBH}} > 0.2$ is adopted to select events with at least one NS. For events with higher P_{BBH}, the systems have larger chirp masses and heavier BHs, where the NS is unlikely to be tidally disrupted unless the BH has a high aligned spin. According to the preliminary online estimates, for NSBH merger candidates, GW 230529_181500 and S250206dm are the most likely to produce EM counterparts, with $P_{\mathrm{HasRemnant}} > 0$ for the two events only. Given the more precise localization, S250206dm is more feasible for current wide-field survey facilities to follow up.

We conducted a follow-up campaign for S250206dm using WFST, installed at the summit of the Saishiteng Mountain near Lenghu (L. Deng et al. 2021), Qinghai province, China. WFST has a field of view (FoV) of 6.55 deg^2 and a 2.5 m primary mirror, making WFST one of the most powerful transient survey facilities in the world (G. Conroy 2023; T. Wang et al. 2023). Extragalactic transients are primary targets for WFST (T. Wang et al. 2023), including GW EM counterparts, supernovae, tidal disruption events, etc. WFST got the first light in 2023 September, a few months after the start of O4. To search for potential EM counterparts of GW events detected in O4, a presearch and delicate follow-up strategy through WFST target of opportunity (ToO) observations was developed in Z.-Y. Liu et al. (2023). The ToO strategy was subsequently applied to observations of GW events S240422ed and S250206dm.

For S250206dm, WFST observations started approximately 14.7 hr (12:10 UTC on 2025 February 7) after the GW detection and lasted for a week (Z. Y. Liu et al. 2025; Z. L. Xu et al. 2025), primarily focused on the northern part of the skymap. To mitigate the effects of moonlight (moon phase of $\sim$0.7, increasing in subsequent nights) and Galactic extinction, a longer-wavelength combination of the r, i, and z bands was adopted. Additionally, given the high density of stars in the low Galactic latitude region of S250206dm skymap, exposure times of 1×90 and 2×60 s for each pointing in each band were adopted to prevent excessive saturation. Pointings with multiple coverages per night were dithered to fill the CCD gap.

The WFST coverage and limiting magnitudes on the first night are shown in Figure 1. To evaluate the search capability, the limiting magnitudes in each band are converted to absolute magnitudes using the median distance estimate from the GW skymap in panels (c), (d), and (e). The effect of Galactic foreground extinction is also included. The host extinction is not considered in this work due to the generally large projected distance from the Galactic center (W.-f. Fong et al. 2022). The extinction correction in this work is based on the $E(B-V)$ map from E. F. Schlafly & D. P. Finkbeiner (2011), with $R_V = 3.1$. For the KN AT 2017gfo, the peak absolute magnitudes are approximately -16 mag in the r, i, and z bands (B. P. Abbott et al. 2017a). With a limiting magnitude range from approximately -15.8 to -18.0 mag, our observations achieve the depth required to detect an AT 2017gfo-like KN at the peak phase.

The observing strategies for the second and third nights were similar to those of the first night. As the potential KN became fainter and the localization was updated, a strategy with a longer exposure time and a smaller coverage area was adopted. Specifically, for the fifth and sixth nights, the reduced coverage region is shown in Figure 2, where the i and z bands with exposure times of 3×120 and 2×180 s were used, respectively. The observation on the fourth night was not

[13] https://online.igwn.org

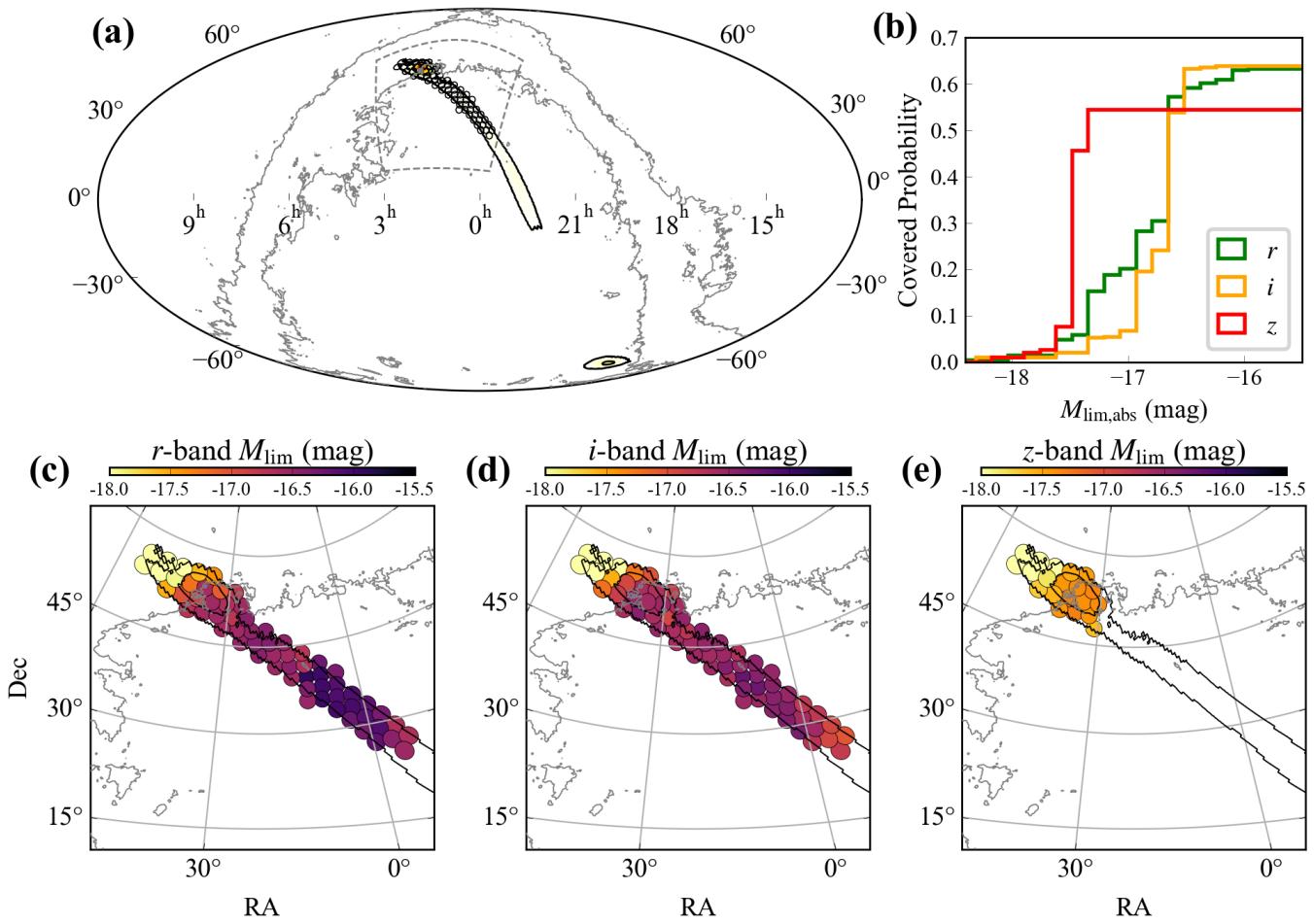

Figure 1. Skymap coverage and multiband depths of WFST on the first night for S250206dm. Panel (a): the total coverage by WFST for S250206dm, where the Bilby skymap of S250206dm from LIGO Scientific Collaboration et al. (2025) is adopted, with 50% and 90% probability region contours. Galactic extinction is also considered, with the contour of $E(B-V)=0.3$ for reference (E. F. Schlafly & D. P. Finkbeiner 2011). Panel (b): the probability coverage by the WFST as a function of limiting absolute magnitudes in the r, i, and z bands. Panels (c), (d), and (e): the zoomed-in covered regions by WFST in the r, i, and z bands, respectively, corresponding to the region delineated by the dashed line in panel (a). The color map represents the 5σ limiting absolute magnitudes after stacking, converted based on the distance estimate for each WFST pointing.

Table 1
Properties of the Significant BNS or NSBH Candidates Discovered in O4

Event	FAR ($\rm yr^{-1}$)	$P_{\rm BNS}$	$P_{\rm NSBH}$	$P_{\rm BBH}$	$P_{\rm HasRemnant}$	A_{90} ($\rm deg^2$)	$D_{\rm L}$ (Mpc)
S230518h	0.10	0%	86%	4%	0%	460	204 ± 57
GW230529_181500[b]	0.0062	31%	62%	0%	12%	24534	197 ± 62
S230627c	0.10	0%	49%	48%	0%	82	291 ± 64
S240910ci	0.10	0%	31%	69%	0%	394	662 ± 166
S241109bn	4.5×10^{-4}	0%	72%	28%	0%	10,138	603 ± 159
S250206dm	0.04	37%	55%	0%	30%	547	373 ± 104
S250818k	2.15	29%	0%	0%	100%	949	237 ± 62

Notes. The information of these candidates is from GRACEDB,[a] where the BNS or NSBH candidates are selected by $P_{\rm BNS}+P_{\rm NSBH}>0.2$.
[a] https://gracedb.ligo.org/
[b] Although the data of GW230529_181500 has been released, the online results of the event property are adopted here to compare with other events.

conducted due to snowy weather at the summit. The covered area, probability, and observation time range for each night are summarized in Table 2. In total, ∼64% and ∼55% of the Bilby skymap (LIGO Scientific Collaboration et al. 2025) were covered by WFST during the first three nights and the last two nights, respectively.

3. Search for EM Counterparts

The raw images from the follow-up observations of S250206dm were processed using the WFST pipeline, which is mainly based on the Vera C. Rubin Observatory/LSST image processing pipeline (hereafter the "LSST pipeline";

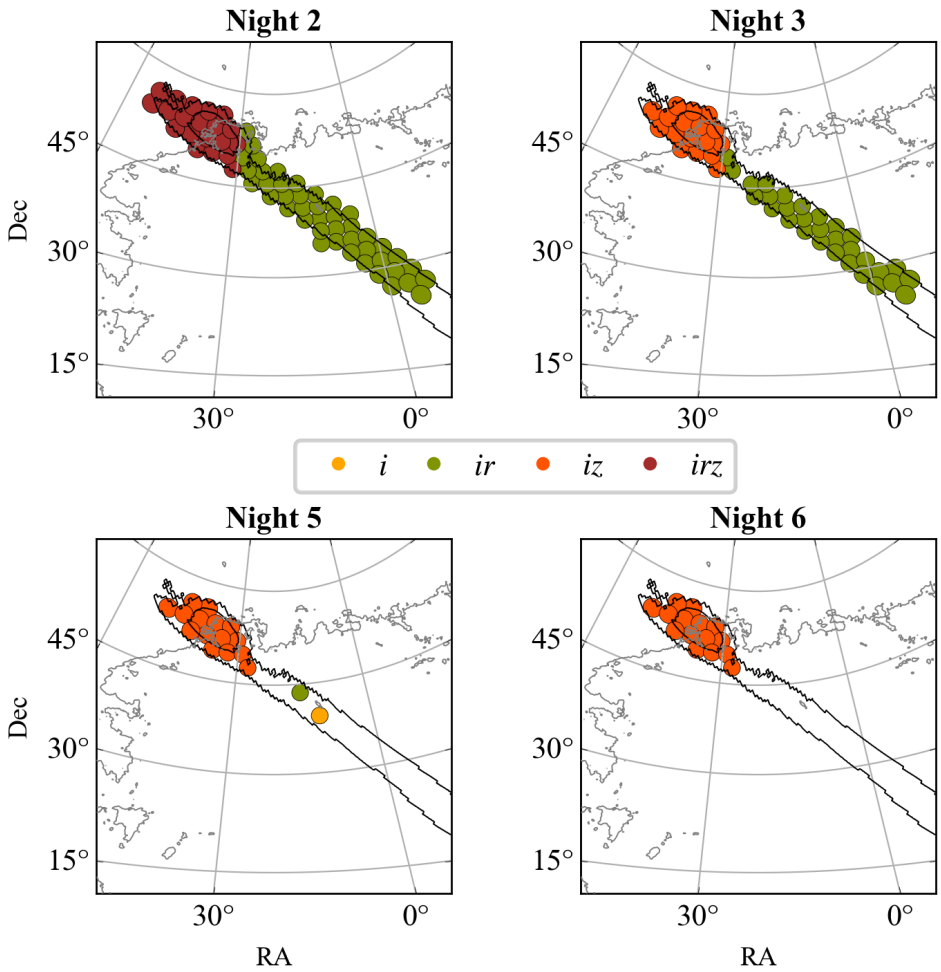

Figure 2. Skymap coverage of WFST observations for S250206dm after the first night. The Bilby skymap of S250206dm from LIGO Scientific Collaboration et al. (2025) is adopted, with 50% and 90% probability region contours shown. Galactic foreground is shown as a contour of $E(B-V) = 0.3$ (E. F. Schlafly & D. P. Finkbeiner 2011).

Table 2
Summary of WFST Follow-up Observations for S250206dm

Night	Start Time (UTC)	End Time (UTC)	Band	Area[a] (deg^2)	$P_{covered}$[a]
1	2025-02-07T12:10:10	2025-02-07T17:01:21	*r*, *i*, *z*	345	∼64%
2	2025-02-08T12:14:53	2025-02-08T17:15:32	*r*, *i*, *z*	345	∼64%
3	2025-02-09T12:14:04	2025-02-09T17:00:05	*r*, *i*, *z*	259	∼63%
4	No observation due to the weather				
5	2025-02-11T13:00:10	2025-02-11T16:49:24	*i*, *z*	97	∼55%
6	2025-02-12T13:28:49	2025-02-12T17:06:47	*i*, *z*	85	∼54%

Note.
[a] Corresponding to the total covered area and probability of all bands, where the FoV of WFST is approximated as a circle with a $1.^{\circ}4$ radius.

J. Bosch et al. 2018). The LSST pipeline is a modular and efficient software suite written in a combination of Python and C++ to process massive survey data. The main processing steps of the LSST pipeline include data ingestion, instrument signature removal, point-spread function (PSF) modeling, astrometric and photometric calibration, source detection and deblending, image alignment and coaddition, image subtraction, and alert product generation. The WFST pipeline was modified from the LSST pipeline in two main aspects: the addition of extension files defining the CCD configuration and the replacement of the subtraction software with `SFFT` to optimize and expedite the subtraction process (L. Hu et al. 2022). Please see M. Cai et al. (2025) for details of the WFST pipeline.

To search for the EM counterpart in a timely manner, despite the lack of WFST archival images for the S250206dm skymap, the preliminary search was conducted using the first night data as reference images, but no valid candidate was found. To ensure that the potential counterpart is faint enough, reference images were taken about 2 weeks later

Table 3
Number of Alerts after a Series of Filters for the Candidate Search

Description	Filter	Alert Number
Total		3746535
Multiple detections	$N_{\rm det} \geqslant 2$	1735634
Real source	$S_{\rm RB} \geqslant 0.1$	93180
Positive source	$N_{\rm negative} = 0$	48771
Not a variable star	$d_{\rm point} \geqslant 1''$	5002
Far from a bright source	$d_{\rm 15mag} \geqslant 10''$, $d_{\rm 12mag} \geqslant 40''$	2236
Not galactic nucleus activity	$d_{\rm nuc} \geqslant 0\farcs5$	2172
Not a moving object	$d_{\rm SkyBot} \geqslant 3''$	2172

(2025-02-16T12:44 to 2025-02-21T14:59 UTC), millions of alerts were detected through basic image reduction, stacking for the images in the same band each night, and subtraction using the WFST pipeline. We searched for the KN using the following filtering criteria to exclude contamination:

1. Not bogus or artifacts: Require multiple detections of $N_{\rm det} \geqslant 2$ and $S_{\rm RB} \geqslant 0.1$, where $S_{\rm RB}$, calculated by a real-bogus (RB) classifier (Y. Liu et al. 2025), represents the fraction of real detections for an alert.
2. Not variable stars: Exclude alerts close to known point sources.
3. Not close to bright sources: Exclude alerts around bright sources ($M < 15$ mag), which may produce false detections due to saturation.
4. Not galactic nucleus activity: Exclude alerts close to centers of known galaxies.
5. Not moving object: Exclude alerts close to known solar system objects.

The number of alerts remained after each filter is shown in Table 3, where crossmatches of variable stars, bright sources, and Galactic centers are performed using Pan-STARRS1 (PS1) DR2 and Gaia DR3 catalogs (K. C. Chambers et al. 2016; E. A. Magnier et al. 2020; Gaia Collaboration et al. 2023). Point and extended sources are distinguished by star classification probability and the difference between the results of PSF and Kron photometry (with sources satisfying $M_{i,\rm PSF} - M_{i,\rm Kron} < 0.05$ classified as stars[14]) for the Gaia and PS1 databases, respectively. To exclude moving objects, the remaining alerts were crossmatched with the Sky Body Tracker to rule out solar system objects (J. Berthier et al. 2006). Finally, 2172 alerts remained after applying an inclusive set of filters to avoid missing potential candidates. These remaining alerts will undergo visual inspection based on analogous criteria described in Table 3 to exclude artifacts and other contamination.

4. Candidate Analysis

After visual inspection of the filtered alerts, 12 candidates were identified as off-nucleus extragalactic transients, as listed in Table 4. To exclude transients that occurred before the GW detection, these candidates were crossmatched with public survey databases, including the Transient Name Server (TNS; A. Gal-Yam 2021), Zwicky Transient Facility (ZTF; E. C. Bellm et al. 2019; M. J. Graham et al. 2019), ALeRCE explorer (F. Förster et al. 2021), and the Asteroid Terrestrial-impact Last Alert System (J. L. Tonry et al. 2018; K. W. Smith et al. 2020) forced photometry server (L. Shingles et al. 2021). Two candidates are excluded as potential counterparts due to archival detections by ZTF. Additionally, assuming the nearest galaxy as the host galaxy, the luminosity distances of the remaining 10 candidates were obtained from the galaxy redshifts by crossmatching them with the GLADE+ catalogs and PS1-based photometric redshift catalogs (R. Beck et al. 2021; G. Dálya et al. 2022). The percentiles of the marginal cumulative distribution function (CDF) at the locations of candidates are listed in Table 4, with four candidates excluded due to significantly larger distances compared with GW localization, even when uncertainties of photometric redshifts are taken into account. For the 12th candidate, the subtraction was re-performed with the archival images of PS1 3π survey as reference (R. Beck et al. 2021) because it is still visible in the WFST template images.

For the remained six candidates, we further compared their absolute magnitudes and variability (after Galactic extinction correction) with the KN model. The WFST lightcurves of the six candidates are shown in Figure 3. The peak absolute magnitudes and evolution of these candidates are shown in Figure 4. The spaces of KNe based on the model `POSSIS` (M. Bulla 2019; S. Anand et al. 2020; M. Bulla 2023) are shown for comparison (for details of the model, please see Section 5). The sampling times of simulated KN lightcurves used to derive absolute magnitudes and variability are $\sim$0.7 and $\sim$2.7 days postmerger, corresponding to the detection times of most candidates. Regarding their evolution, the decay rates of these six candidates are slower than those of KNe produced by BNS mergers but consistent with the range of decay rates for NSBH mergers. In terms of luminosity, all candidates are brighter than the luminosity range derived from the model, where the luminosity distance is set as 373 Mpc due to no spectroscopic redshift available for these candidates. Two candidates (the eighth and ninth) have peak magnitudes close to those of the simulated KN sample when the uncertainty of their photometric redshifts is considered. However, it remains challenging to classify them as KN candidates due to their limited number of detections. For other candidates, to produce such a bright KN, additional energy sources beyond radioactive decay are required, such as central engine activity (Y.-W. Yu et al. 2013). Some magnetar-enhanced KN candidates associated with sGRBs have been discovered (H. Gao et al. 2017), but no valid enhanced KN has been confirmed to date. Additionally, the merger remnant of S250206dm is unlikely to be a magnetar in the case of a BNS merger, due to its large chirp mass, which tends to collapse directly into a BH.

To analyze the possibility as the afterglow counterpart of S250206dm for these six candidates, the scenarios of the BNS and NSBH merger are discussed as follows, respectively. For a BNS merger, the afterglow lightcurves with various viewing angles are simulated using the model `afterglowpy` (G. Ryan et al. 2020), where the best-fitting results in G. Ryan et al. (2020) of the GRB 170817A afterglow are adopted for other model parameters. Producing an afterglow with similar luminosity to the candidates requires a small viewing angle ($\theta_{\rm obs} < 3^\circ$), but the evolution of such an afterglow is quite fast compared with the candidate lightcurves. For an NSBH merger, if these candidates originated from the afterglow, their slow evolutions correspond to the afterglow peak phase.

[14] https://outerspace.stsci.edu/display/PANSTARRS/How+to+separate+stars+and+galaxies

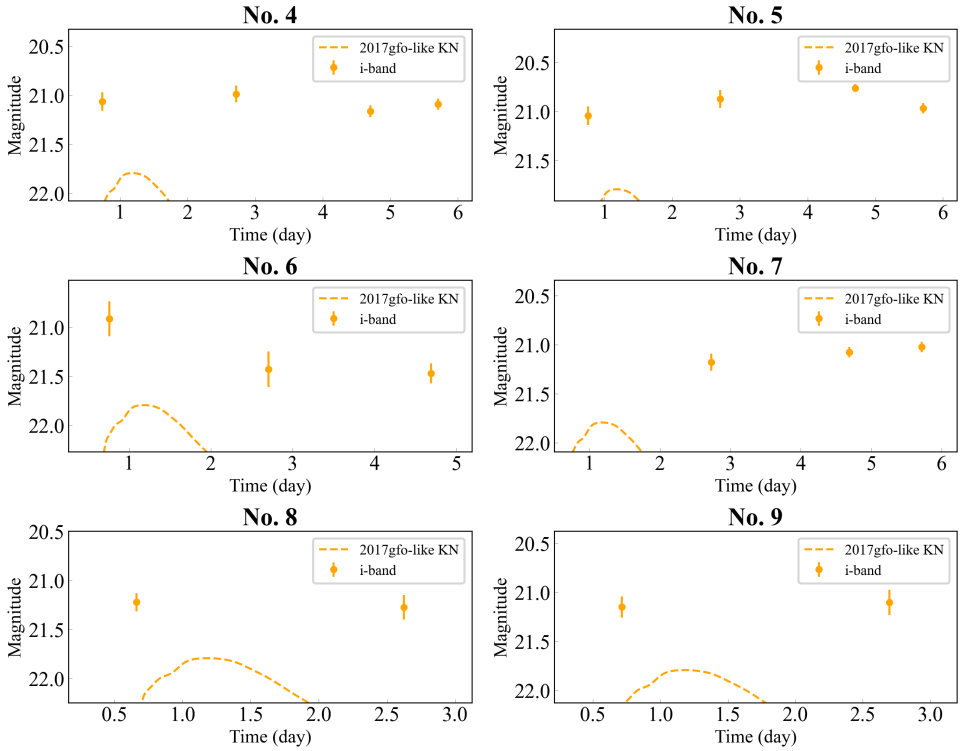

Figure 3. Lightcurves of the six WFST candidates tagged "too bright" or "slow evolution." The luminosity distance of a 2017gfo-like KN is set as the median of 373 Mpc.

Table 4
Properties of 12 Candidates after Human Vetting and Specific Reasons for Exclusion as a KN Counterpart

No.	$N_{\rm det}$[a]	R.A.	Decl.	$\dot{M}_i$[b] (mag day^{-1})	Band	$M_{i,\rm p}$[b] (mag)	$M'_{i,\rm p}$[c] (mag)	$D_{\rm L,host}$[d] (Mpc)	CDF($D_{\rm L}$)[e]	Offset (Kpc)	Reason
1	7	40.01920	50.88298	0.08 ± 0.03	r, i, z	-16.7 ± 0.5	-17.4 ± 0.5	395 ± 75[b]	0.63	7.5	Previous detection
2	4	356.20686	28.06492	0.22 ± 0.11	r, i	-19.2 ± 0.1	-19.4 ± 0.1	446	0.54	5.5	Previous detection
3	4	35.91705	53.46289	0.02 ± 0.03	i	-18.6 ± 0.3	-19.0 ± 0.3	780 ± 81[a]	0.94	15.2	Skymap mismatched
4	4	30.12691	48.66882	0.00 ± 0.03	i	-18.3 ± 0.7	-18.7 ± 0.7	705 ± 203[a]	0.99	2.7	Slow evolution
5	4	29.93754	51.35800	-0.02 ± 0.03	i	-18.1 ± 0.7	-18.5 ± 0.7	589 ± 193[a]	0.98	4.1	Slow evolution
6	3	30.88382	49.36016	0.14 ± 0.07	i	-19.1 ± 0.7	-19.6 ± 0.7	990 ± 225[a]	1.00	4.5	Too bright
7	3	38.80782	56.26273	-0.05 ± 0.05	i	-17.3 ± 0.4	-18.5 ± 0.4	473 ± 76[a]	0.86	7.1	Slow evolution
8	2	3.45112	32.29102	0.03 ± 0.11	i	-17.1 ± 0.4	-17.2 ± 0.4	471 ± 76[a]	0.62	4.7	Too bright?
9	2	4.47506	32.98365	-0.02 ± 0.12	i	-17.3 ± 0.5	-17.4 ± 0.5	472 ± 76[a]	0.64	1.2	Too bright?
10	2	40.15301	53.50889	0.02 ± 0.03	i	-20.5 ± 0.6	-21.4 ± 0.6	2158 ± 504[b]	1.00	3.5	Skymap mismatched
11	3	32.21519	53.05843	0.03 ± 0.03	i	-20.6 ± 0.5	-21.0 ± 0.5	1789 ± 377[b]	0.99	3.4	Skymap mismatched
12	12	35.70140	50.28884	0.03 ± 0.01	r, i, z	-20.4 ± 0.6	-21.05 ± 0.6	1727 ± 375[b]	0.99	4.4	Skymap mismatched

Notes.
[a] Total number of detections of each candidate, after stacking of images with the same band each night. All uncertainties are given at the 1σ level.
[b] The magnitude changing rate and peak absolute magnitude of each candidate are listed in the i band. The error of peak absolute magnitudes includes the uncertainties of the host distances.
[c] The peak absolute magnitude of each candidate after Galactic extinction correction.
[d] The spectroscopic redshift result of the No. 2 candidate is from DESI DR1 (DESI Collaboration et al. 2025). Distance with marker "a" is based on the photometric redshifts collected in the GLADE+ catalog (G. Dálya et al. 2022). If there is no match with the GLADE+ catalog, the host distance is based on the photometric redshift result of the PS1 survey (R. Beck et al. 2021), and is marked with "b."
[e] The cumulative conditional probability given the host distance and the candidate 2D location, based on the Bilby skymap. For candidates excluded by "skymap mismatched," the host distance of $\mu - 3\sigma$ is adopted to show the deviation while considering the uncertainty of the photometric redshifts.

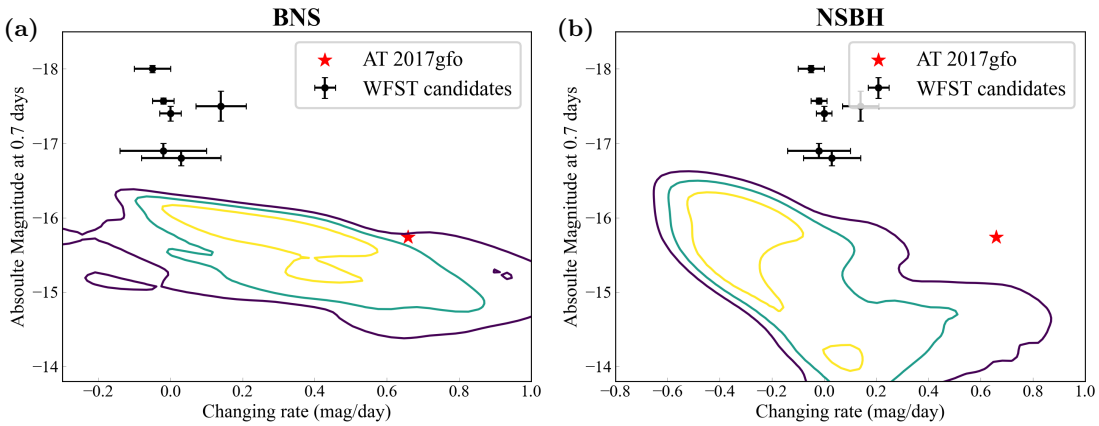

Figure 4. The model-dependent space of peak magnitude and variability in the *i* band. Panels (a) and (b): the KN model POSSIS is adopted for simulating KNe in the BNS and NSBH mergers, respectively. The black dots and red pentacles represent the six candidates tagged "too bright" or "slow evolution" and AT 2017gfo, respectively. To derive the absolute magnitude, the luminosity distance is set as 373 Mpc for the candidates with no spectroscopic redshift available. Three contour lines correspond to the 50th, 90th, and 99 percentiles of the KN model regions.

According to

$$t_{\mathrm{peak},i} \simeq 1.2 \times 10^3 (1+z) \left(\frac{E_{\mathrm{K},i}}{10^{53}\ \mathrm{erg}}\right)^{(1/3)} \left(\frac{n}{1\ \mathrm{cm}^{-3}}\right)^{(-1/3)} \left(\frac{\Gamma_i}{50}\right)^{(-8/3)} \mathrm{s}, \quad (1)$$

$t_{\mathrm{peak},i} \approx 2$ days corresponds to a slow Lorentz factor ($\Gamma_i < 5$), where $E_{\mathrm{K},i} = 10^{55}$ erg and $n = 0.1\ \mathrm{cm}^{-3}$ (B. Zhang 2018). However, such a slow Lorentz factor is inconsistent with a jet from an NSBH merger due to a limited baryon loaded. Therefore, these six candidates are unlikely to be related to the KN or afterglow counterpart of S250206dm. No spectral follow-up was carried out to further confirm the 12 candidates due to their faint brightnesses (mostly > 21 mag) and reasons for exclusion.

Candidates reported in the community were also checked in the WFST data. These candidates in the optical band are from the ZTF team (T. Ahumada et al. 2025) and TNS.[15] Candidates reported by the GW MultiMessenger Astronomy Dark Energy Camera (DECam; B. Flaugher et al. 2015) survey team (L. Hu et al. 2025) are not included due to limited overlap in the covered regions between WFST and Wendelstein. The coverage and detection of candidates by WFST are listed in Table 6 in the Appendix, where candidates reported before the GW detection time and with decl. $\leqslant 0°$ are not included. It is not surprising that most candidates were not detected in the WFST difference images, due to the short time interval of approximately 2 weeks between the science and the reference images. Based on this time interval, the WFST follow-up observations are not sensitive to sources with slow evolution. For example, the candidate AT 2025bay, reported by ZTF, has a magnitude difference of ∼0.2 mag in the *r* band between the time of obtaining WFST science images and that of reference images, according to the lightcurve in T. Ahumada et al. (2025). This variability, corresponding to ∼22.5 mag in WFST difference images, is near the detection limit of WFST. Such sources with slow evolution are faint and difficult to detect in the WFST observations. Based on WFST detections, no candidate is likely to be a KN counterpart. Additionally, in the X-ray band, candidates reported by the Einstein Probe through GCN Circulars (D. Y. Li et al. 2025) were also checked in our data. However, no valid extragalactic source was discovered within the positional error of the candidates. Consequently, no robust KN candidate was discovered in the WFST follow-up observations.

[15] https://www.wis-tns.org/ligo/o4/S250206dm_20250206_212530

5. Counterpart Constraint and Insights into Origin

Although nondetection of EM counterparts of GW events, the KN luminosity, ejecta mass during merger, and merger system property can be constrained by follow-up observations assuming a KN model (K. Ackley et al. 2020; S. Anand et al. 2020; M. M. Kasliwal et al. 2020; M. Pillas et al. 2025). A state-of-the-art KN model POSSIS is adopted in our analysis. POSSIS is a radiative transfer code for KNe developed by M. Bulla (2019), including dynamical ejecta produced by collisions and tidal interactions, as well as disk wind ejecta generated by outflows from the postmerger accretion disk. For a BNS merger, postmerger ejecta and dynamical ejecta are distributed near the polar axis and the equatorial plane, respectively. As the grid model is based on simulations, the velocity ranges of dynamical and postmerger ejecta are fixed at 0.1–0.3*c* and 0.025–0.1*c*, respectively. The free parameters of the model include dynamical ejecta mass M_{dyn}, postmerger ejecta mass M_{pm}, half-opening angle of the dynamical ejecta θ_{open}, and viewing angle θ_{obs}. A surrogate model from K. Lukošiute et al. (2022) is adopted to obtain results for arbitrary parameters in our calculations.

For AT 2017gfo-like KNe, the lightcurves are produced using POSSIS with the parameters from the fitted results in T. Dietrich et al. (2020): $M_{\mathrm{dyn}} = 0.005\,M_\odot$, $M_{\mathrm{pm}} = 0.052\,M_\odot$, $\theta_{\mathrm{open}} = 49.^\circ5$, and $\theta_{\mathrm{obs}} = 42.^\circ8$. For general BNS mergers, the ranges of dynamical ejecta M_{dyn} and postmerger ejecta M_{pm} are 0.0025–0.02 $M_\odot$ and 0.01–0.1 $M_\odot$, respectively. For NSBH mergers, the ranges of M_{dyn} and M_{pm} are both 0.01–0.09 $M_\odot$. For BNS and NSBH mergers, θ_{open} are fixed at 45° and 30° according to M. Bulla (2019) and S. Anand et al. (2020), respectively, and θ_{obs} are both sampled uniformly. Additionally, the distance and the viewing angle are randomly combined in our analysis due to the lack of further estimates from the GW signal.

For a BNS merger origin, the constraint results based on POSSIS are shown in the left two panels of Figure 5.

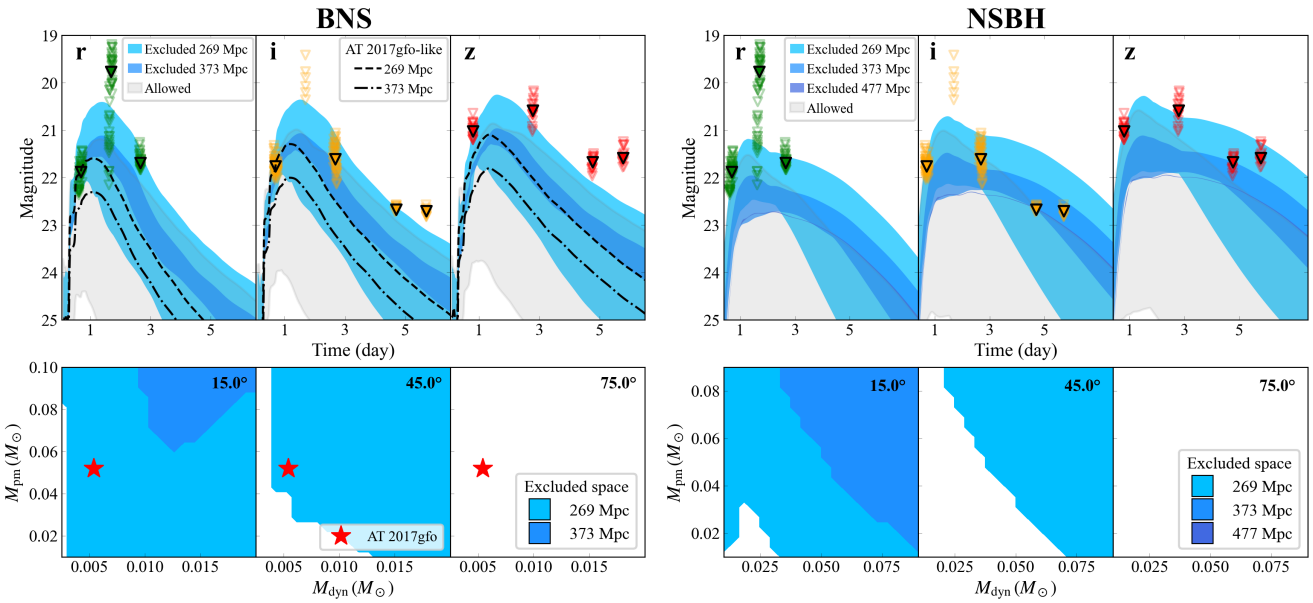

Figure 5. Parameters constraints based on the nondetection result, assuming a BNS (left) or an NSBH merger (right) for S250206dm. The two top panels show constraints on KN luminosity derived using the `POSSIS` model at different distances (corresponding to the median and $\pm1\sigma$ distances from Bilby skymap). The 5σ limiting magnitude of each WFST pointing and the median magnitudes are plotted with open and solid inverted triangles, respectively. Galactic extinction with a median $E(B-V)=0.1$ is applied in all panels. Light/deep blue and gray regions represent excluded and allowed KN scenarios, respectively. For the BNS merger, black dashed and dashed–dotted lines represent AT 2017gfo-like KNe generated using `POSSIS` at 269 and 373 Mpc, respectively. The two bottom panels show constraints on ejecta mass. Three viewing angles of 15°, 45°, and 75° are adopted. The fitted ejecta masses of AT 2017gfo from T. Dietrich et al. (2020) are plotted as a red star for the BNS merger.

As shown in the top-left panel of Figure 5, lightcurves of the AT 2017gfo-like KN and other simulated KNe from various parameter combinations are compared with WFST detection upper limits after considering Galactic extinction. The constraint mainly depends on observations of the first three nights due to the fast evolution of KNe from BNS mergers. At 269 Mpc, an AT 2017gfo-like KN can be ruled out by our observations in both the r and i bands, and most parameter combinations can also be excluded. The corresponding ejecta mass of the excluded lightcurves is shown in the bottom-left panel of Figure 5. As the viewing angle ($\theta_{\rm obs}$) or distance ($D_{\rm L}$) increases, KNe become fainter, leading to a broader range of allowed ejecta masses. Based on the ejecta mass estimate of AT 2017gfo (T. Dietrich et al. 2020), an AT 2017gfo-like KN is ruled out at 269 Mpc, with a viewing angle of $\theta_{\rm obs} < 45°$. At $\theta_{\rm obs} = 45°$ and $D_{\rm L} = 269$ Mpc, the masses of postmerger and dynamical ejecta are constrained to $M_{\rm pm} \lesssim 0.03\,M_\odot$ and $M_{\rm dyn} \lesssim 0.01\,M_\odot$, respectively. These mass upper limits are consistent with the ejecta produced in a scenario in which a BNS merger directly collapses into a BH.

For an NSBH merger origin, similar results to BNS are also shown in the right two panels of Figure 5. KN lightcurves with bright peaks but rapid decay or faint peaks but slow decay are ruled out by the first and the fifth night observations, respectively. The WFST observations can effectively constrain KN lightcurves up to the median distance of 373 Mpc. As shown in the bottom-right panel of Figure 5, at $\theta_{\rm obs} = 45°$ and $D_{\rm L} = 269$ Mpc, a total ejecta mass greater than $\sim 0.1\,M_\odot$ is ruled out. In the optimistic scenario ($\theta_{\rm obs} = 15°$, $D_{\rm L} = 269$ Mpc), the masses of postmerger and dynamical ejecta can be further constrained to $M_{\rm pm} \lesssim 0.03\,M_\odot$ and $M_{\rm dyn} \lesssim 0.03\,M_\odot$, respectively.

In comparison with `POSSIS`, we also employ another KN model, `SuperNu`, for the NSBH merger. `SuperNu` is a Monte Carlo radiative transfer code (R. T. Wollaeger et al. 2019, 2021; O. Korobkin et al. 2021), assuming a two-component axisymmetric ejecta that includes dynamical and wind ejecta (similar to postmerger ejecta in `POSSIS`, hereafter

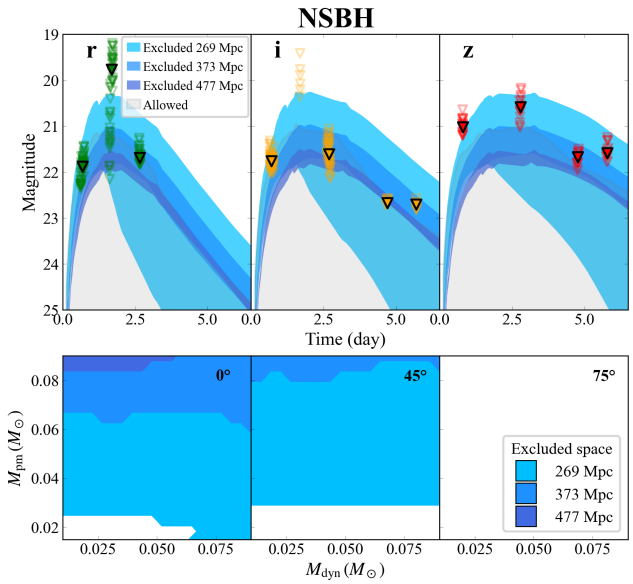

Figure 6. Parameters constraint assuming an NSBH merger for S250206dm, similar to Figure 5, but based on the `SuperNu` KN model. The top and bottom panels show the constraints on simulated KN lightcurves and ejecta masses produced during the merger, respectively. The `SuperNu` NSBH model and three luminosity distances (corresponding to the median and $\pm1\sigma$ distances from Bilby skymap) are adopted. Galactic extinction with a median $E(B-V)=0.1$ is adopted. In the top panel, the 5σ limiting magnitude of each WFST pointing and the median magnitudes are plotted with hollow and solid inverted triangles, respectively. In the bottom panel, three viewing angles of 0°, 45°, and 75° are adopted.

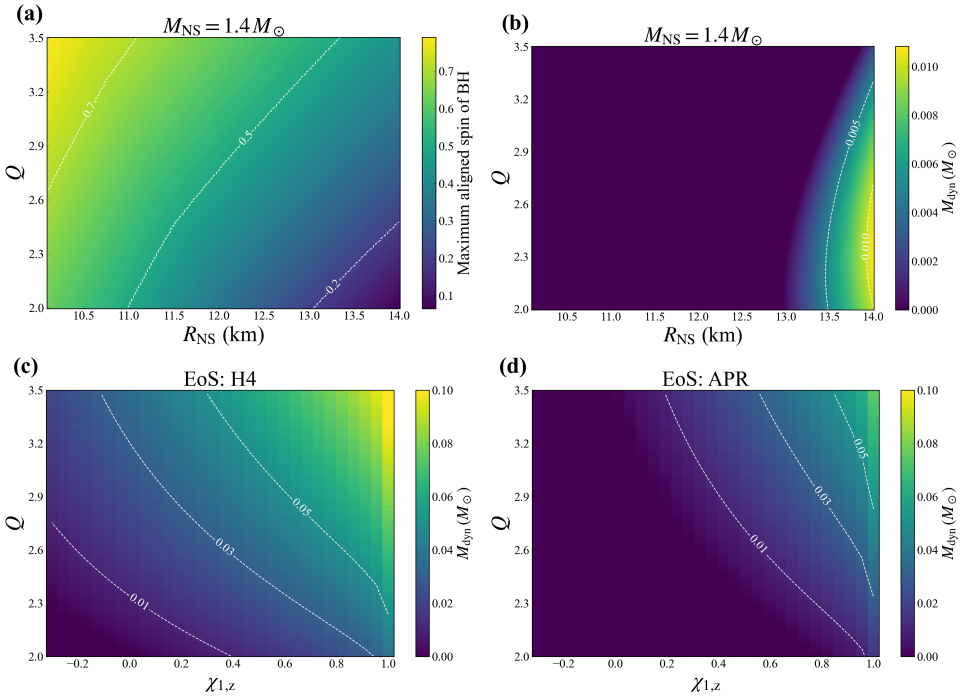

Figure 7. The nondetection constraints on the mass ratio (Q) and aligned spin of the BH ($\chi_{1,z}$) for S250206dm. In panels (a) and (b), the NS mass is set as 1.4 $M_\odot$, and the white dashed lines represent the contour of the allowed maximum aligned spin of the BH and the mass of dynamical ejecta, respectively. In panel (a), the maximum aligned spin of the BH derived from ejecta mass limits, where an optimistic result of $M_{\rm wind} \lesssim 0.03\ M_\odot$ and $M_{\rm dyn} \lesssim 0.03\ M_\odot$ is adopted. In panel (b), a BH with zero aligned spin in the system is adopted. In panels (c) and (d), the EoSs of H4 and APR are adopted to calculate the produced dynamical ejecta mass, respectively. The white dashed lines represent the contour of the mass of dynamical ejecta produced during the merger. The system chirp mass is set as 1.8 $M_\odot$, derived from the source classification probability of S250206dm.

also referred to as postmerger ejecta). A grid of simulation results is calculated using `SuperNu` with varying masses, velocities, morphologies, and compositions. In our calculations, a surrogate model for `SuperNu` from A. Kedia et al. (2023) is adopted. Similar to the NSBH case in `POSSIS`, a morphology (named "TSwind2" in A. Kedia et al. 2023) is adopted for KNe produced by an NSBH merger, including a torus-shaped dynamical ejecta and a spherical postmerger ejecta. To reduce the model's degrees of freedom, the velocities of the dynamical and postmerger ejecta are set to 0.18c and 0.06c, respectively, corresponding to the average velocities derived from the velocity distribution of the `POSSIS` NSBH model. The ejecta mass ranges for the two components are both 0.01–0.09 $M_\odot$. The constraint results, similar to those in Figure 5, are shown in Figure 6. Compared with `POSSIS`, the trends of the results are similar, and the constraints weaken as the distance or viewing angle increases. For `SuperNu`, the KN lightcurves are more sensitive to $M_{\rm pm}$: at a distance of 269 Mpc and a viewing angle of 45°, $M_{\rm pm} < 0.03\ M_\odot$ is derived from our observational upper limits, but with no effective constraint on $M_{\rm dyn}$. Overall, the constraint on $M_{\rm pm}$ is tighter than that for `POSSIS`, whereas the opposite holds for $M_{\rm dyn}$.

Combined with the numerical simulation results of BNS and NSBH mergers, the derived constraints on ejecta mass can be used to further infer the properties of the progenitor (I. Andreoni et al. 2020; M. W. Coughlin et al. 2020; S. Anand et al. 2020). For a BNS merger origin for S250206dm, a large chirp mass leads to direct collapse into a BH during the merger. It is challenging to infer the merger system due to the theoretically small amount of ejecta. Therefore, we only consider the NSBH merger case here. The empirical equations from numerical simulation results, as used in B. P. Gompertz et al. (2023) and M. Pillas et al. (2025), are adopted here to derive $M_{\rm dyn}$ and $M_{\rm pm}$ for the progenitor. Specifically, Equation (9) in C. J. Krüger & F. Foucart (2020) is used to calculate $M_{\rm dyn}$. The total ejecta mass, $M_{\rm rem}$, is estimated using Equation (4) in F. Foucart et al. (2018), where $M_{\rm rem} = M_{\rm disk} + M_{\rm dyn}$. The postmerger (wind) ejecta mass is obtained by a fraction ξ of disk material converted into wind ejecta, where ξ is related to the binary mass ratio and can be estimated using Equation (12) in G. Raaijmakers et al. (2021). In our calculations, the H4 and Akmal–Pandharipande–Ravenhall (APR) equations of state (EoSs) are adopted, with their $R_{1.4}$ and $M_{\rm TOV}$ values being (13.7 km, 2.03 $M_\odot$) and (11.3 km, 2.19 $M_\odot$), representing a "stiff" and a "soft" equation of state (EoS), respectively.

Derived from WFST observations, the constraints on the aligned spin of the BH ($\chi_{1,z}$) and the system mass ratio ($Q = M_{\rm BH}/M_{\rm NS}$) are shown in Figure 7. In panels (a) and (b), the NS masses are both assumed to be $M_{\rm NS} = 1.4\,M_\odot$. An optimistic result of $M_{\rm pm} \lesssim 0.03\,M_\odot$ and $M_{\rm dyn} \lesssim 0.03\,M_\odot$ is used to derive the upper limit on $\chi_{1,z}$, corresponding to $\theta_{\rm obs} = 15°$ and $D_{\rm L} = 269$ Mpc. The produced dynamical ejecta mass, given the mass ratio and NS radius, is shown in panel (b), where a BH with zero aligned spin is assumed, according to low-aligned spin measurements of BH for most NSBH merger candidates detected to date (see Table 5). Compared with the constraint of $M_{\rm dyn} \lesssim 0.03\,M_\odot$ from the follow-up observations, it is challenging to derive an informative constraint on mass ratio and NS radius only by WFST observations.

When combined with the GW signal, similar results are shown in panels (c) and (d) of Figure 7, where the system chirp mass is set to $M_{\rm c} = 1.8\,M_\odot$, estimated from a source

Table 5
Properties of S250206dm and Other Published NSBH Merger Events or Candidates

Event[a]	m_1 ($M_\odot$)	m_2 ($M_\odot$)	χ_{1z}	D_L (Mpc)	M_{dyn}[b] ($M_\odot$)	M_{wind} ($M_\odot$)	$M_{lim,abs}$[c] (mag)	P_c	References
GW190426_152155	$6.2^{+1.8}_{-1.6}$	$1.6^{+0.4}_{-0.3}$	$-0.04^{+0.19}_{-0.29}$	370^{+180}_{-160}	⋯	⋯	−16.4	52%	M. M. Kasliwal et al. (2020)
GW190814	$24.4^{+0.7}_{-0.6}$	$2.72^{+0.05}_{-0.05}$	$-0.00^{+0.02}_{-0.02}$	240^{+40}_{-50}	⋯	⋯	−14.9	99%	K. Ackley et al. (2020)
GW191219_163120	$34.7^{+1.3}_{-1.4}$	$1.30^{+0.04}_{-0.03}$	$-0.00^{+0.04}_{-0.05}$	550^{+250}_{-160}	⋯	⋯	⋯	⋯	⋯
GW200105_162426	$9.6^{+0.6}_{-0.7}$	$2.02^{+0.11}_{-0.09}$	$-0.00^{+0.05}_{-0.06}$	270^{+120}_{-110}	⋯	⋯	−17.2	52%	S. Anand et al. (2020)
GW200115_042309	$6.3^{+1.3}_{-1.8}$	$1.53^{+0.48}_{-0.20}$	$-0.15^{+0.16}_{-0.38}$	290^{+150}_{-100}	⋯	⋯	−15.8	22%	S. Anand et al. (2020)
GW230529_181500	$3.8^{+0.51}_{-0.75}$	$1.49^{+0.31}_{-0.15}$	$-0.11^{+0.12}_{-0.19}$	201^{+102}_{-96}	⋯	0.001(–)	−16.0	16%	M. Pillas et al. (2025)
S250206dm[d]	3.84	1.20	0	373^{+104}_{-104}	0.029(–)	0.009(0.001)	−16.1	64%	WFST (this work)
	3.19	1.40	0		0.008(–)	0.010(–)			
	2.73	1.60	0		⋯	0.004(–)			
	3.84	1.20	0.8		0.070(0.038)	0.070(0.052)			
	3.19	1.40	0.8		0.035(0.010)	0.087(0.059)			
	2.73	1.60	0.8		0.008(–)	0.089(0.052)			
S250206dm							−17.4	68%	ZTF (T. Ahumada et al. 2025)
							−15.2	9.3%	DECam (L. Hu et al. 2025)
							−17.5	4.9%	T80S (L. Hu et al. 2025)

Notes.
[a] The information on published GW events is from the posterior distribution results in R. Abbott et al. (2021, 2023) and A. G. Abac et al. (2024).
[b] The ejecta mass produced is calculated assuming the EoS of H4 (APR). $R_{1.4}$ and M_{TOV} for EoSs H4 and APR are (13.7 km, 2.03 $M_\odot$) and (11.3 km, 2.19 $M_\odot$), respectively. The marker "⋯" represents the produced ejecta less than $1 \times 10^{-3}\,M_\odot$.
[c] The best median limiting magnitudes from multiple bands and the first three nights are adopted. The median limiting magnitude of DECam on the seventh night is adopted, as observations began on that night.
[d] The chirp mass of $\sim$1.8 $M_\odot$is adopted, estimated based on the source classification probability of S250206dm. Assuming a nonrotating NS, M_{TOV} is used to distinguish between NS and BH in our calculations.

classification probability of S250206dm using the method in M. Pillas et al. (2025). The method is described as follows: An estimate of source classifications in some GW online search pipelines, such as PyCBC Live, is based on the method in V. Villa-Ortega et al. (2022). Estimation primarily depends on the measurement of the chirp mass, assuming an astrophysical origin of the event, a correct distance estimate, and a point estimate of the source's detector frame chirp mass by template matching. The latest source classifications estimated by PyCBC Live are 37% and 55% for a BNS merger and an NSBH merger, respectively. Therefore, the chirp mass of S250206dm is derived using the inverse process of the method in V. Villa-Ortega et al. (2022), combined with the event distance estimate. Assuming minimum and maximum NS masses of 1 and 3 $M_\odot$, respectively, a source chirp mass of $\sim$1.8 $M_\odot$ is estimated for S250206dm. For the H4 (N. K. Glendenning & S. A. Moszkowski 1991) and APR (A. Akmal et al. 1998) EoSs, the region with $M_{dyn} \gtrsim 0.03\,M_\odot$ is excluded based on the observation-derived constraint, indicating that an NSBH with a large mass ratio and a high aligned spin is disfavored by our observations. Even for a BH with a low-aligned spin ($\chi_{1,z} = 0$), a large mass ratio ($Q \gtrsim 3.2$) is still disfavored assuming a "stiff" EoS like H4.

To assess the ability of optical follow-ups in constraining the properties of merger systems, we compare the GW posterior distributions of $\chi_{1,z}$ and Q with the constraints derived from optical observations as shown in Figure 8. For NSBH mergers involving a massive black hole (BH $>5\,M_\odot$), such as GW190814 and GW200105_162426, optical data provide limited constraints. In contrast, for events located within the mass gap like S250206dm, WFST observing constraints reach into the GW posterior of most NSBH candidates. This optical-derived constraint achieves, for the first time, a precision comparable to that inferred from the GW signal, thereby complementing the GW estimate. The result shows that follow-up observations with limiting magnitudes of 22–23 mag can effectively constrain the mass ratio, aiding in distinguishing between a heavy BNS and an NSBH system for mass-gap events.

6. Other ToO Observations and Joint Constraints

Due to its importance and rarity, for S250206dm, ground-based wide-field survey facilities, such as ZTF and DECam, around the world have participated in the EM counterpart search (T. Ahumada et al. 2025; L. Hu et al. 2025; G. S. H. Paek et al. 2025; K. W. Smith et al. 2025; R. Stein et al. 2025). However, no valid EM counterpart has been reported by the community. Information on some published follow-up observations is listed in Table 5, including ZTF (T. Ahumada et al. 2025) and DECam (L. Hu et al. 2025). WFST observations covered a comparable area (64%) to ZTF (68%), but with a detection limit of (−16.1 mag), which is $\sim$1.3 mag deeper than that of ZTF (−17.4 mag). Although WFST's limiting magnitude is shallower than that of DECam (−15.2 mag), its coverage is more timely and significantly wider compared to DECam, which began $\sim$6 days after the GW detection and covered an area of 10%. Additionally, at 269 Mpc, AT 2017gfo-like KNe can be excluded only by WFST observations, as shown in Figure 9. To derive the detection efficiency for AT 2017gfo-like KNe at different positions, we performed a quantitative analysis by randomly sampling $\sim$19,000 positions (R.A., decl., and luminosity distance) according to the Bilby skymap (LIGO Scientific Collaboration et al. 2025) of S250206dm using the `dynesty` sampler (J. Skilling 2004; J. S. Speagle 2020;

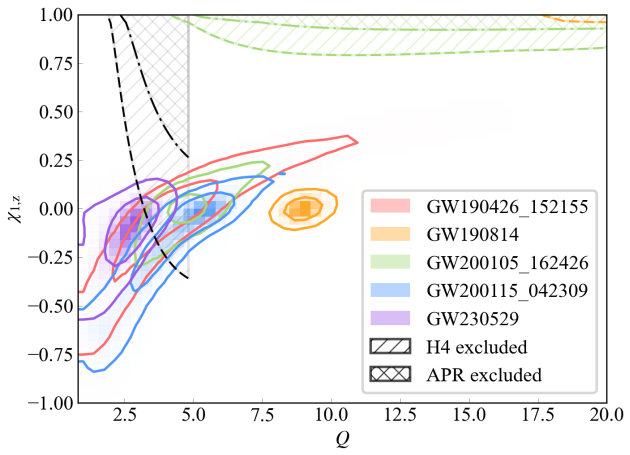

Figure 8. The constraints on the merger system from optical follow-ups compared with GW posterior estimates. With the chirp mass (M_c) fixed, the shaded areas with diagonal line and crosses represent the excluded spaces of the mass ratio (Q) and aligned spin of the BH ($\chi_{1,z}$) under EoSs of H4 and APR, respectively. Q is restricted by the minimum NS mass assumed to be 1 $M_\odot$. The gray shaded areas are ruled out space for S250206dm in this work, assuming M_c as 1.8 $M_\odot$ and an optimistic constraint of $M_{\rm dyn} \lesssim 0.03\ M_\odot$. For GW190814 and GW200105_162426, the constrains are also shown based on the optimistic upper limits on $M_{\rm dyn}$ (S. Anand et al. 2020; I. Andreoni et al. 2020) and M_c estimates (R. Abbott et al. 2021, 2023) of ($\lesssim$0.001 $M_\odot$, 6.1 $M_\odot$) and ($\lesssim$0.02 $M_\odot$, 3.4 $M_\odot$), respectively. The contours represent the published GW posterior estimates of NSBH candidates at 50% and 90% confidence (R. Abbott et al. 2021, 2023; A. G. Abac et al. 2024).

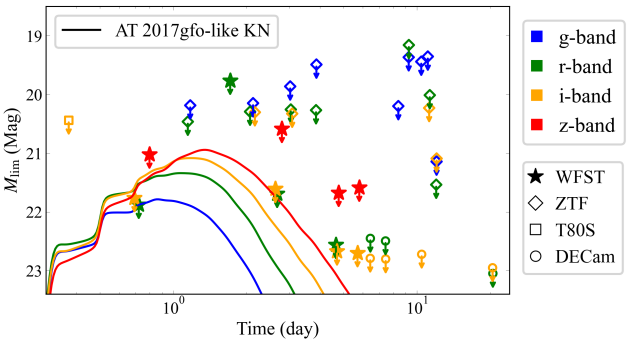

Figure 9. Survey depths of WFST and other optical wide-field survey facilities for S250206dm. Lightcurves of AT 2017gfo-like KNe at 269 Mpc and median apparent 5σ limiting magnitudes in different bands are represented by solid lines and scatter, respectively. The ZTF data are reported in T. Ahumada et al. (2025), and the T80S and DECam data are reported in L. Hu et al. (2025). Although the regions covered by DECam and T80S focus on the skymap in the southern sky and do not overlap with ZTF and WFST, their depths are also plotted for comparison. Galactic extinction is not considered here.

S. Koposov et al. 2025). Detection is determined by comparing the luminosity of simulated KNe and 5σ limiting magnitudes of WFST observations. Under the requirement of at least one detection in any band, the derived detection ratios under conditions with and without Galactic extinction are ∼34% and ∼10%, respectively. Therefore, in terms of both depth and coverage, WFST has conducted the best follow-up observations of S250206dm to our knowledge, thanks to the powerful capability of WFST and the great observing conditions at the Lenghu site (L. Deng et al. 2021).

Combining the results of other ToO observations helps constrain the potential KN counterpart due to complementarity in observation times and the regions covered by different telescopes. For S250206dm, the ZTF observations effectively supplement the monitoring of the northern skymap 1–2 days after the merger, when WFST has relatively shallow depth due to cloudy weather (as shown in Figure 9). Combined with ZTF data, the joint constraints on the KN luminosity for BNS and NSBH mergers are shown in panels (a) and (b) in Figure 10 in the Appendix, respectively. For the BNS merger, some bright scenarios are excluded by the ZTF data. The strengthening of constraint is limited for both BNS and NSBH merges due to the difference in depth between WFST and ZTF. Additionally, the joint constraint combining with DECam and T80S data is inappropriate due to the lack of overlap in the regions covered by WFST. However, these observations increase the reliability (covered probability increases from 64% to 74%) of the assumption in the model constraint that the merger occurred within the observed field.

7. Conclusion

In this work, we conducted timely follow-up observations by WFST and a detailed EM counterpart search for the GW event S250206dm, which is the first well-localized NS merger candidate potentially located in the mass gap. Lasting for a week, WFST observations covered ∼64% of the localization region in the r, i, z bands, with a 5σ limiting magnitude up to 23 mag. After data reduction and the candidate search, 12 off-nucleus extragalactic transients are discovered, but they are unlikely to be the KN or the afterglow related to S250206dm based on the analysis of the host and photometric evolution. Compared with other ToO observations, the WFST follow-up for S250206dm is superior in both depth and coverage.

According to the observation limit, an AT 2017gfo-like KN counterpart to S250206dm at 267 Mpc can only be excluded by WFST. Combined with the KN model `POSSIS`, the ejecta mass is constrained as $M_{\rm pm} \lesssim 0.03\,M_\odot$ and $M_{\rm dyn} \lesssim 0.01\,M_\odot$ for a BNS merger; $M_{\rm pm} \lesssim 0.03\,M_\odot$ and $M_{\rm dyn} \lesssim 0.03\,M_\odot$ for an NSBH merger, assuming the condition of a near on-axis observation and at 269 Mpc. Furthermore, the mass ratio of progenitor and aligned spin of the BH are also constrained for NSBH merger. Compared with the estimate from the GW signal, the constraint on the mass ratio through the optical follow-up can reach a similar order of accuracy for the first time. Our results show that rapid, deep follow-up observations are capable of constraining the properties of compact binary progenitors, providing crucial constraints on the nature of the mass gap.

The WFST observations of S250206dm indicate the potential capacity of WFST in searching for a KN counterpart (Z.-Y. Liu et al. 2023). Due to its unique geographical location, WFST can enhance the counterpart search of GW skymaps in the northern hemisphere. Combined with ZTF and Pan-STARRS, WFST is able to complement the wide-field survey facilities in the southern hemisphere, such as DECam and LSST. Looking forward, with the participation of WFST and LSST in the GW EM counterpart search in the upcoming O5,[16] breakthroughs on compact binary mergers within the mass gap are expected to be achieved.

[16] https://observing.docs.ligo.org/plan/

Acknowledgments

The WFST is a joint facility of the University of Science and Technology of China, Purple Mountain Observatory. We appreciate the members of the WFST operation and maintenance team for their support. This work was supported by the National Key R&D Program of China (grant No. 2023YFA1608100), the National Natural Science Foundation of China (grant Nos. 12393812, 12325301 and 12273035), the Strategic Priority Research Program of the Chinese Academy of Science (grant No. XDB0550300), the National Key R&D Program of China (grant Nos. 2021YFC2203102 and 2022YFC2204602), and Cyrus Chun Ying Tang Foundations.

Software: `astropy` (Astropy Collaboration et al. 2013, 2018; Astropy Collaboration et al. 2022); `SciPy` (P. Virtanen et al. 2020); `NumPy` (C. R. Harris et al. 2020); `Matplotlib` (J. D. Hunter 2007); `SWarp` (E. Bertin 2010); `dustmap` (G. M. Green 2018); `ligo.skymap` (L. P. Singer et al. 2016a, 2016b); `HOTPANTS` (A. Becker 2015); `afterglowpy` (G. Ryan et al. 2020); `dynesty` (J. Skilling 2004; J. S. Speagle 2020; S. Koposov et al. 2025).

Author Contributions

Z.Y.L. conducted most of the analyses and wrote the manuscript under the supervision of W.Z. W.Z., and Z.P.J., and Z.G.D. initiated this study. Z.L.X., J.A.J., L.L.F., M.X.C., and L.H. contributed to the data reduction pipeline of WFST. J.A.J., Z.Y.L., Z.L.X., W.Y.W., D.Z.M., J.H.Z., K.X.Y., and Z.Q.J. contributed to the human inspection of the candidate search. R.D.L., L.H., J.J.G., and D.X. helped with and discussed the model analyses. T.G.W., X.K., X.F.W., Q.F.Z., Y.Q.X., J.A.J., N.J., Y.X.Z., H.F.Z., M.L., D.Z.Y., B.L., X.Z. Z., F.L., H.L., X.L.Z., J.L.T., H.R.W., Z.W., and J.W. contributed to the development of WFST. All of the authors contributed to the discussion.

Appendix

The results of the combined constraints with ZTF and the search for reported candidates based on WFST data are included in the Appendix, as shown in Figure 10 and Table 6, respectively.

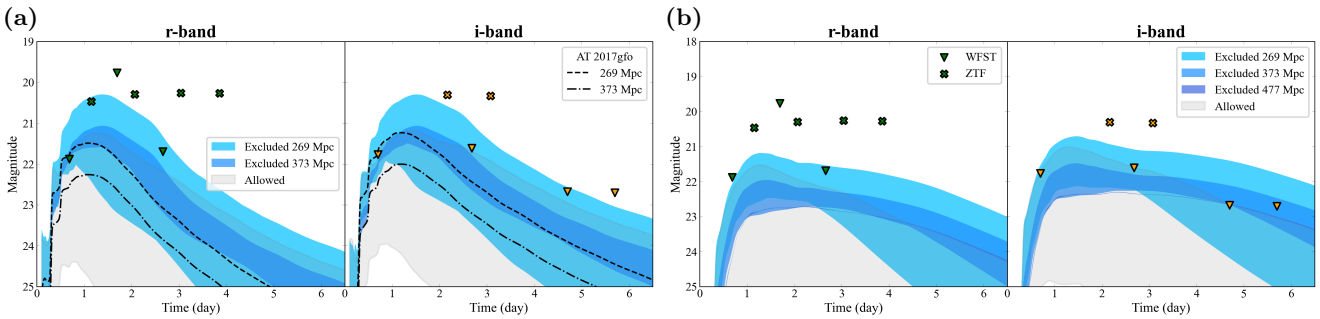

Figure 10. Joint constraints on KN luminosity, similar to the top two panels in Figure 5, but combining ZTF observations. Panels (a) and (b) correspond to BNS and NSBH mergers, respectively. The median limiting magnitudes of WFST and ZTF are represented by inverted triangles and crosses, respectively.

Table 6
Cross-checked Results of Reported Candidates Based on WFST Follow-up Data

TNS Name[a]	R.A.	Decl.	Coverage	Detection	Team
AT 2025bcq	36.31265	50.17796	Yes	Yes	ZTF
AT 2025bda	354.33854	22.97904	No	No	ZTF
AT 2025bay	7.504874	37.16833	Yes	No	ZTF
AT 2025brm	359.26723	29.48768	Yes	Yes	ZTF
AT 2025ben	356.32103	28.02299	Yes	Yes	ZTF
AT 2025bro	356.59715	28.65744	Yes	No	ZTF
AT 2025brn	2.03711	32.84554	Yes	No	ZTF
AT 2025bcx	7.35227	38.69038	Yes	No	ZTF
AT 2025bcw	21.33198	45.27197	Yes	No	ZTF
AT 2025brp	358.69192	32.65047	Yes	No	ZTF
AT 2025brl	1.90744	27.96404	Yes	Yes	ZTF
AT 2025bcr	20.49131	48.97043	No	No	ZTF
AT 2025bew	31.57170	53.01039	Yes	No	Pan-STARRS
AT 2025bey	25.75487	45.46341	No	No	Pan-STARRS
AT 2025bex	24.46251	45.33960	No	No	Pan-STARRS
AT 2025bev	30.24625	52.32467	Yes	No	Pan-STARRS
AT 2025bcc	32.02902	55.34248	Yes	No	Pan-STARRS
AT 2025bbt	45.46907	51.12973	No	No	Pan-STARRS
AT 2025bbo	24.32197	45.72550	Yes	No	Pan-STARRS
AT 2025bbn	37.78844	50.73533	Yes	No	Pan-STARRS
AT 2025bbm	36.96265	49.47591	Yes	No	Pan-STARRS
AT 2025bwl	357.78800	34.19678	No	No	Pan-STARRS
AT 2025bce	31.23239	54.79534	Yes	No	Pan-STARRS
AT 2025bbl	7.12748	33.19370	No	No	Pan-STARRS
AT 2025bmq	38.51758	54.57247	Yes	Yes	WL-GW
AT 2025azn	39.82257	49.57253	Yes	No	SAGUARO
AT 2025azm	2.03128	32.56575	Yes	No	SAGUARO

Note.
[a] Candidates with decl. $\leqslant 0°$ are not included, which are far from the region covered by WFST.

ORCID iDs

Zhengyan Liu https://orcid.org/0000-0002-2242-1514
Ji-an Jiang https://orcid.org/0000-0002-9092-0593
Wen Zhao https://orcid.org/0000-0002-1330-2329
Zhiping Jin https://orcid.org/0000-0003-4977-9724
Zigao Dai https://orcid.org/0000-0002-7835-8585
Xuefeng Wu https://orcid.org/0000-0002-6299-1263
Daming Wei https://orcid.org/0000-0002-9758-5476
Runduo Liang https://orcid.org/0000-0001-6223-840X
Lei He https://orcid.org/0000-0001-7613-5815
Minxuan Cai https://orcid.org/0000-0003-4721-6477
Lulu Fan https://orcid.org/0000-0003-4200-4432
Weiyu Wu https://orcid.org/0009-0003-9474-8457
Jinjun Geng https://orcid.org/0000-0001-9648-7295
Di Xiao https://orcid.org/0000-0002-4304-2759
Jian Wang https://orcid.org/0000-0003-1617-2002
Hongfei Zhang https://orcid.org/0000-0002-1463-9070
Hairen Wang https://orcid.org/0000-0002-4372-0759
Lei Hu https://orcid.org/0000-0001-7201-1938
Xu Kong https://orcid.org/0000-0002-7660-2273
Bin Li https://orcid.org/0000-0001-9327-0920
Ning Jiang https://orcid.org/0000-0002-7152-3621
Tinggui Wang https://orcid.org/0000-0002-1517-6792
Zhen Wan https://orcid.org/0000-0002-3105-3821
Yongquan Xue https://orcid.org/0000-0002-1935-8104
Qingfeng Zhu https://orcid.org/0000-0003-0694-8946
Xianzhong Zheng https://orcid.org/0000-0003-3728-9912

References

Abac, A. G., Abbott, R., Abouelfettouh, I., et al. 2024, ApJL, 970, L34
Abbott, B. P., Abbott, R., Abbott, T. D., et al. 2017a, ApJL, 848, L12
Abbott, B. P., Abbott, R., Abbott, T. D., et al. 2017b, PhRvL, 119, 161101
Abbott, B. P., Abbott, R., Abbott, T. D., et al. 2017c, Natur, 551, 85
Abbott, R., Abbott, T. D., Abraham, S., et al. 2021, PhRvX, 11, 021053
Abbott, R., Abbott, T. D., Acernese, F., et al. 2023, PhRvX, 13, 041039
Ackley, K., Amati, L., Barbieri, C., et al. 2020, A&A, 643, A113
Ahumada, T., Anand, S., Bulla, M., et al. 2025, arXiv:2507.00357
Akmal, A., Pandharipande, V. R., & Ravenhall, D. G. 1998, PhRvC, 58, 1804
Anand, S., Coughlin, M. W., Kasliwal, M. M., et al. 2020, NatAs, 5, 46
Andreoni, I., Goldstein, D. A., Kasliwal, M. M., et al. 2020, ApJ, 890, 131
Astropy Collaboration, Price-Whelan, A. M., Lim, P. L., et al. 2022, ApJ, 935, 167
Astropy Collaboration, Price-Whelan, A. M., Sipőcz, B. M., et al. 2018, AJ, 156, 123
Astropy Collaboration, Robitaille, T. P., Tollerud, E. J., et al. 2013, A&A, 558, A33
Barbieri, C., Salafia, O. S., Colpi, M., et al. 2019, ApJL, 887, L35
Beck, R., Szapudi, I., Flewelling, H., et al. 2021, MNRAS, 500, 1633
Becker, A. 2015, HOTPANTS: High Order Transform of PSF ANd Template Subtraction, Astrophysics Source Code Library, ascl:1504.004
Bellm, E. C., Kulkarni, S. R., Graham, M. J., et al. 2019, PASP, 131, 018002
Berthier, J., Vachier, F., Thuillot, W., et al. 2006, ASPC, 351, 367
Bertin, E. 2010, SWarp: Resampling and Co-adding FITS Images Together, Astrophysics Source Code Library, ascl:1010.068
Bosch, J., AlSayyad, Y., Armstrong, R., et al. 2018, ASPC, 523, 521
Bulla, M. 2019, MNRAS, 489, 5037
Bulla, M. 2023, MNRAS, 520, 2558
Cai, M., Xu, Z., Fan, L., et al. 2025, arXiv:2501.15018
Chambers, K. C., Magnier, E. A., Metcalfe, N., et al. 2016, arXiv:1612.05560
Conroy, G. 2023, Natur, Epub ahead of print
Coughlin, M. W., Dietrich, T., Antier, S., et al. 2020, MNRAS, 492, 863
Coulter, D. A., Foley, R. J., Kilpatrick, C. D., et al. 2017, Sci, 358, 1556
Dálya, G., Díaz, R., Bouchet, F. R., et al. 2022, MNRAS, 514, 1403
D'Avanzo, P., Campana, S., Salafia, O. S., et al. 2018, A&A, 613, L1

Deng, L., Yang, F., Chen, X., et al. 2021, Natur, 596, 353
Dietrich, T., Coughlin, M. W., Pang, P. T. H., et al. 2020, Sci, 370, 1450
DESI Collaboration, Abdul-Karim, M., Adame, A. G., et al. 2025, arXiv:2503.14745
Eichler, D., Livio, M., Piran, T., & Schramm, D. N. 1989, Natur, 340, 126
Flaugher, B., Diehl, H. T., Honscheid, K., et al. 2015, AJ, 150, 150
Fong, W.-f., Nugent, A. E., Dong, Y., et al. 2022, ApJ, 940, 56
Förster, F., Cabrera-Vives, G., Castillo-Navarrete, E., et al. 2021, AJ, 161, 242
Foucart, F., Hinderer, T., & Nissanke, S. 2018, PhRvD, 98, 081501
Gaia Collaboration, Vallenari, A., Brown, A. G. A., et al. 2023, A&A, 674, A1
Gal-Yam, A. 2021, AAS Meeting , 237, 423.05
Gao, H., Zhang, B., Lü, H.-J., & Li, Y. 2017, ApJ, 837, 50
Glendenning, N. K., & Moszkowski, S. A. 1991, PhRvL, 67, 2414
Goldstein, A., Veres, P., Burns, E., et al. 2017, ApJ, 848, L14
Gompertz, B. P., Nicholl, M., Smith, J. C., et al. 2023, MNRAS, 526, 4585
Graham, M. J., Kulkarni, S. R., Bellm, E. C., et al. 2019, PASP, 131, 078001
Green, G. M. 2018, JOSS, 3, 695
Harris, C. R., Millman, K. J., van der Walt, S. J., et al. 2020, Natur, 585, 357
Hu, L., Cabrera, T., Palmese, A., et al. 2025, ApJL, 990, L46
Hu, L., Wang, L., Chen, X., & Yang, J. 2022, ApJ, 936, 157
Hunter, J. D. 2007, CSE, 9, 90
Kasen, D., Metzger, B., Barnes, J., Quataert, E., & Ramirez-Ruiz, E. 2017, Natur, 551, 80
Kasliwal, M. M., Anand, S., Ahumada, T., et al. 2020, ApJ, 905, 145
Kawaguchi, K., Shibata, M., & Tanaka, M. 2020, ApJ, 889, 171
Kedia, A., Ristic, M., O'Shaughnessy, R., et al. 2023, PhRvR, 5, 013168
Koposov, S., Speagle, J., Barbary, K., et al. 2025, joshspeagle/dynesty: v3.0.0, Zenodo, doi:10.5281/zenodo.17268284
Korobkin, O., Wollaeger, R., Fryer, C., et al. 2021, ApJ, 910, 116
Krüger, C. J., & Foucart, F. 2020, PhRvD, 101, 103002
Lattimer, J. M., Mackie, F., Ravenhall, D. G., & Schramm, D. N. 1977, ApJ, 213, 225
Lattimer, J. M., & Schramm, D. N. 1974, ApJL, 192, L145
Li, D. Y., Hu, J. W., Wu, Q. Y., et al. 2025, GCN, 39545, 1
LIGO Scientific CollaborationVIRGO CollaborationKagra Collaboration, et al. 2025, GCN, 39231, 1
Liu, Y., Fan, L., Hu, L., et al. 2025, A&A, 693, A105
Liu, Z. Y., He, L., Zhao, W., et al. 2025, GCN, 39249, 1
Liu, Z.-Y., Lin, Z.-Y., Yu, J.-M., et al. 2023, ApJ, 947, 59
Lukošiute, K., Raaijmakers, G., Doctor, Z., Soares-Santos, M., & Nord, B. 2022, MNRAS, 516, 1137
Magnier, E. A., Schlafly, E. F., Finkbeiner, D. P., et al. 2020, ApJS, 251, 6
Mali, U., & Essick, R. 2025, arXiv:2511.19393
Metzger, B. D. 2020, LRR, 23, 1
Nakar, E. 2020, PhR, 886, 1
Paek, G. S. H., Im, M., Jeong, M., et al. 2025, GCN, 39241, 1
Pian, E., D'Avanzo, P., Benetti, S., et al. 2017, Natur, 551, 67
Pillas, M., Antier, S., Ackley, K., et al. 2025, PhRvD, 112, 083002
Planck Collaboration, Aghanim, N., Akrami, Y., et al. 2020, A&A, 641, A6
Raaijmakers, G., Nissanke, S., Foucart, F., et al. 2021, ApJ, 922, 269
Ryan, G., Eerten, H., Piro, L., & Troja, E. 2020, ApJ, 896, 166
Savchenko, V., Ferrigno, C., Kuulkers, E., et al. 2017, ApJL, 848, L15
Schlafly, E. F., & Finkbeiner, D. P. 2011, ApJ, 737, 103
Shappee, B. J., Simon, J. D., Drout, M. R., et al. 2017, Sci, 358, 1574
Shingles, L., Smith, K. W., Young, D. R., et al. 2021, TNSAN, 7, 1
Singer, L. P., Chen, H.-Y., Holz, D. E., et al. 2016a, ApJL, 829, L15
Singer, L. P., Chen, H.-Y., Holz, D. E., et al. 2016b, ApJS, 226, 10
Skilling, J. 2004, AIPC, 735, 395
Smith, K. W., Angus, C. R., Young, D. R., et al. 2025, GCN, 39211, 1
Smith, K. W., Smartt, S. J., Young, D. R., et al. 2020, PASP, 132, 085002
Speagle, J. S. 2020, MNRAS, 493, 3132
Stein, R., Karambelkar, V., Frostig, D., et al. 2025, GCN, 39256, 1
Tanvir, N. R., Levan, A. J., González-Fernández, C., et al. 2017, ApJL, 848, L27
Tonry, J. L., Denneau, L., Heinze, A. N., et al. 2018, PASP, 130, 064505
Troja, E., Piro, L., Van Eerten, H., et al. 2017, Natur, 551, 71
Villa-Ortega, V., Dent, T., & Curiel Barroso, A. 2022, MNRAS, 515, 5718
Virtanen, P., Gommers, R., Oliphant, T. E., et al. 2020, NatMe, 17, 261
Wang, T., Liu, G., Cai, Z., et al. 2023, SCPMA, 66, 109512
Wollaeger, R. T., Fryer, C. L., Chase, E. A., et al. 2021, ApJ, 918, 10
Wollaeger, R. T., Fryer, C. L., Fontes, C. J., et al. 2019, ApJ, 880, 22
Xu, Z. L., Meng, D. Z., Liu, Z. Y., et al. 2025, GCN, 39293, 1
Yu, Y.-W., Zhang, B., & Gao, H. 2013, ApJ, 776, L40
Zhang, B. 2018, The Physics of Gamma-Ray Bursts (Cambridge Univ. Press)